Materials Advances

ROYAL SOCIETY OF CHEMISTRY

PAPER

View Article Online
View Journal



Cite this: DOI: 10.1039/d5ma01527h

# Extraction of Schottky diode parameters and electron transport and dielectric relaxation in $PdSe_2$ nanoflakes

Tooba Nazir,[a] Qaisar Abbas,[ab] Syed Mesam Tamar Kazmi,[ab] Chuanbo Li,[c] Xiulai Xu[de] and M. A. Rafiq*[bf]

Received 29th December 2025,
Accepted 28th March 2026

DOI: 10.1039/d5ma01527h

rsc.li/materials-advances

Palladium diselenide ($PdSe_2$) exhibits a unique anisotropic electronic behavior, high carrier mobility, and layer-dependent indirect-to-direct bandgap transition, positioning it as a versatile material for next-generation 2D device architectures. In this work, we investigated the electrical properties and conduction and relaxation mechanisms of mechanically exfoliated $PdSe_2$ flakes. Raman spectroscopy and AFM were employed to confirm the purity and thickness of the sample. Electrical characterizations, including current–voltage ($I$–$V$) measurements and complex impedance spectroscopy (CIS) were performed, revealing crucial information about charge carrier transport mechanisms, contact behavior, and resistive properties. For contact-limited conduction mechanisms, Schottky emission was investigated, and the thermionic emission model was employed to determine the Schottky diode parameters, along with a re-evaluation of Richardson's constant. In bulk-limited conduction mechanisms, the Poole–Frenkel (PF) emission was ascertained with a determination of the dielectric constant. To gain insights into the relaxation mechanisms, complex impedance spectroscopy, complex dielectric permittivity, and complex modulus spectroscopy analyses were conducted. A switching ratio of $\sim 10^2$ was achieved, indicating the suitability of $PdSe_2$ for applications in memory devices, neuromorphic computing, and sensing technologies.



## Introduction

Recent advances in materials science have placed nanomaterials at the center stage of scientific and technological innovation, with atomically thin 2D transition metal dichalcogenides (TMDCs) emerging as a major focus of current research. This attention has roots in the vast array of applications ranging from electronics and optoelectronics to sensing, catalysis and flexible devices. Unlike their bulk counterparts, TMDCs give access to highly tunable optical, electronic, chemical and mechanical properties.[1–3] Among TMDCs, noble metal dichalcogenides (NMDCs) exhibit distinctive properties, including thickness-dependent electronic structures, remarkable air stability, unusual electronic phase transitions and, in some cases, even superconductivity.[4] These materials have the general chemical formula $MX_2$, where M is a noble metal from group 10 (Pd or Pt) and X is a chalcogen (S or Se).[4]

Within the family of NMDCs, $PdSe_2$ draws attention as it is characterized by an orthorhombic phase, resulting in an in-plane anisotropy and a layered, puckered pentagonal structure.[5] These features make it exhibit striking electronic-band-structure characteristics, such as a transition between semiconducting and metallic behavior with the change in the number of layers. Also, $PdSe_2$ exhibits high air stability,[5] a tunable bandgap[6] and robust photoresponse properties,[7] and thus, it is an appealing material to be incorporated in infrared photodetectors, field-effect transistors, and gas sensors.[8] Notably, $PdSe_2$ holds advantages over other group 10 dichalcogenides; for example, it combines the durability of $PdTe_2$ under ambient exposure with the band tunability of $PtSe_2$ while maintaining the thermodynamic stability that limits $PdS_2$. This unique combination places $PdSe_2$ as a more versatile and durable candidate for probing polarization phenomena, promoting its integration into next-gen optoelectronic and sensing devices.[9] However, the performance and reliability of these devices are strongly influenced by the underlying charge-transport processes, making it necessary to understand the conduction of charges across $PdSe_2$ layers for achieving efficient and stable devices. This understanding can be achieved through detailed AC and DC analyses of the conduction mechanisms. Despite the advances in $PdSe_2$

[a] Department of Physics and Applied Mathematics, Pakistan Institute of Engineering and Applied Sciences, PO Nilore, Islamabad 45650, Pakistan
[b] Condensed Matter Physics Laboratories, Center for Mathematical Sciences, PIEAS, Islamabad 45650, Pakistan. E-mail: aftab@cantab.net
[c] School of Science, Minzu University of China, Beijing 100081, China
[d] Institute of Physics, Chinese Academy of Sciences, Beijing 100190, China
[e] State Key Laboratory for Mesoscopic Physics and Frontiers Science Center for Nano-optoelectronics, School of Physics, Peking University, Beijing 100871, China
[f] National Center for Physics, Islamabad, Pakistan

applications, simultaneous systematic studies of its AC and DC transport mechanisms remain relatively limited, highlighting the need for deeper investigation.

In this work, we address this gap by systematically investigating the conduction mechanisms in mechanically exfoliated nanoflakes of $PdSe_2$ with silver contacts by performing temperature-dependent *I–V* characteristics, complex impedance spectroscopy and complex dielectric permittivity analyses, along with a brief complex modulus spectroscopy analysis. The observation of the non-linear behavior in the *I–V* plot of $PdSe_2$ was consistent with the behavior of Schottky-type contacts. The Schottky diode parameters were evaluated using the thermionic emission model, and a modified value of Richardson's coefficient for Ag/$PdSe_2$/Ag was obtained. Analysis using the Poole–Frenkel emission model enabled the extraction of the dielectric permittivity constant of $PdSe_2$. The temperature and frequency dependence of the impedance in $PdSe_2$ was examined using complex impedance spectroscopy (CIS) analysis to elucidate the underlying charge transport and relaxation processes. Complex dielectric spectroscopy analysis showed strong frequency and temperature dependence in permittivity ($\varepsilon'$), dielectric loss ($\varepsilon''$), and the complex modulus ($M^*$), all of which provided evidence for localized carrier relaxation. This work not only expands the fundamental understanding of $PdSe_2$ but also highlights its potential as a robust candidate for future nano-electronic and optoelectronic applications.

## Materials and methods

Bulk $PdSe_2$ crystals synthesized *via* the chemical vapor transport (CVT) technique were acquired from 6Carbon Technology, China. Interdigitated electrode arrays (IDAs) used for device fabrication were obtained from MicruX Technologies. Each IDA consisted of silver electrodes patterned on a glass substrate, arranged in an interdigitated comb-like configuration with individual finger dimensions of 10 μm × 10 μm.

$PdSe_2$ flakes with controlled thickness and lateral dimensions were mechanically exfoliated from the bulk crystals using thermal release tape (TRT). The exfoliation tape was gently pressed onto the target silicon substrate to ensure strong adhesion, followed by controlled thermal delamination, resulting in reliable transfer and adhesion of the exfoliated $PdSe_2$ flake onto the substrate surface.

The $PdSe_2$ flake with a thickness of approximately 4 nm was transferred onto a silver-contacted IDA using TRT and subjected to temperature-dependent *I–V* measurements in a cryogenic probe station of an Agilent 4156C semiconductor analyzer at a temperature range of 293 K–393 K maintained using liquid nitrogen. Moreover, AC transport measurements were made using an LCR meter 4980A in a frequency range of 200 Hz to 2 MHz at temperatures of 293 K–343 K, with the temperature being controlled using liquid nitrogen.

## Results and discussions

Mechanically exfoliated $PdSe_2$ flakes of desired thickness were subjected to structural characterizations (Fig. 1). Raman spectroscopy was employed to investigate the structural and vibrational characteristics of the $PdSe_2$. Fig. 1(a) shows the Raman spectrum of the bulk $PdSe_2$, whereas Fig. 1(b) illustrates a distinct blueshift in the characteristic peaks, reflecting a reduced interlayer coupling and stronger confinement effects, corresponding to a decrease in the number of layers. The few-layered sample exhibited all 3 A ($A_g^1$, $A_g^2$, and $A_g^3$) modes but only two B ($B_{1g}^1$ and $B_{1g}^2$) modes. This is because the $B_{1g}^3$ mode is very close to the $A_g^3$ mode. Raman analysis validated the high phase purity of the synthesized $PdSe_2$, evidenced by the absence of any peaks attributed to impurity. The observed vibrational modes correspond closely to those reported for crystalline $PdSe_2$, confirming the material's structure and integrity.[8] The sharpness and intensity of these peaks confirmed the crystalline nature of the sample and validated the successful transfer of a high-quality flake onto the substrate. The peaks observed in the lower-frequency region at 75 $cm^{-1}$, 100 $cm^{-1}$ and 125 $cm^{-1}$ are due to the symmetry variations of $PdSe_2$. Absence of any background signals shows that the material is structurally intact and set for subsequent electrical characterizations.

For $PdSe_2$, the flake was exfoliated using TRT and placed onto silicon wafers to perform AFM. Fig. 1(c) shows the visuals of the sample, and Fig. 1(d) shows the recorded deflection of the cantilever. A monolayer of $PdSe_2$ exhibits an average thickness of approximately 0.71 nm.[10] The recorded value of the height profile obtained from atomic force microscopy (AFM) measurements for $PdSe_2$ shows that the thickness of the flake is ~4 nm, which is an equivalent of nearly 5 layers.

The schematic in Fig. 2(a) depicts that the device prepared as a flake is transferred onto a comb-like, 10 μm-spaced, interdigitated silver electrode of an IDA. Fig. 2(b) exhibits the *I–V* characteristic plots for the $PdSe_2$ flake with silver contacts in a temperature range of 293 K–393 K. The non-linear behavior of the curves becomes more pronounced upon an increase in temperature, which is consistent with the semiconducting behavior. The switching ratio being $\sim 10^2$ makes the material a reasonable candidate for analog synaptic elements in neuromorphic devices, high-voltage sensors and high-voltage resistive switching devices.[11–13]

In Fig. 3(a), the Schottky emission characteristics were analyzed by plotting $\ln(I)$ and $\sqrt{V}$ over the temperature range of 343 K–398 K. In the Schottky emission, the current is governed by the thermionic emission of charge carriers across the metal–semiconductor junction, where the electrons are excited to energy levels high enough to surmount the potential barrier. The thermionic emission of electrons is expressed as follows:[14]

$$I = AA^*T^2 \exp\left\{\frac{e\left(\varphi_b - \sqrt{\frac{eV}{4\pi\varepsilon_0\varepsilon_r Ad}}\right)}{k_B T}\right\}, \quad (1)$$

where $A$ is the effective area, $A^*$ is the Richardson's constant, $V$ is the applied voltage, $\varphi_b$ is the barrier height, $d$ is the distance between the contacts, $\varepsilon_0$ is the free space permittivity constant and $\varepsilon_r$ is the dielectric permittivity. Applied voltages below 1.1 V

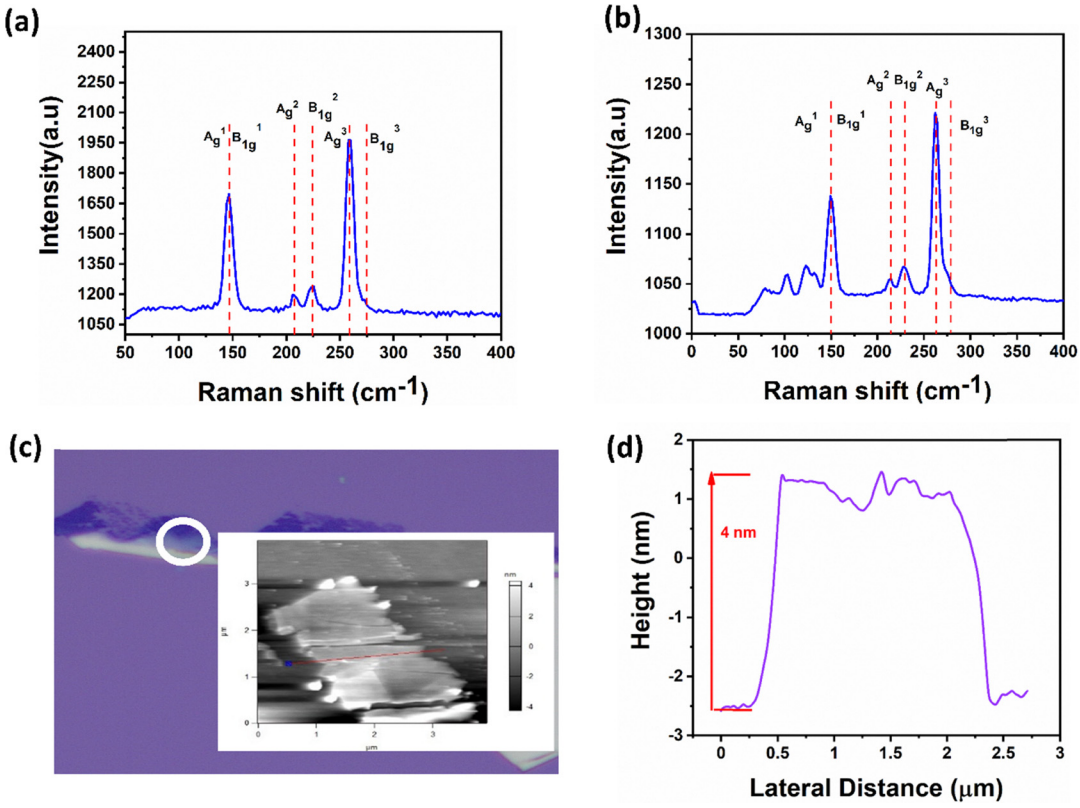


Fig. 1 (a) Raman spectrum of the bulk $PdSe_2$ showing the characteristic vibrational modes corresponding to the bulk phase. (b) Raman spectrum of the mechanically exfoliated few-layered $PdSe_2$ flake, confirming layer reduction *via* blue shifts. (c) AFM image showing the magnified region of the exfoliated $PdSe_2$ flake used for thickness measurement. The selected area highlights the region analyzed to determine the layer thickness of the flake. (d) AFM height profile of the exfoliated few-layered $PdSe_2$ flake on a $Si/SiO_2$ substrate.

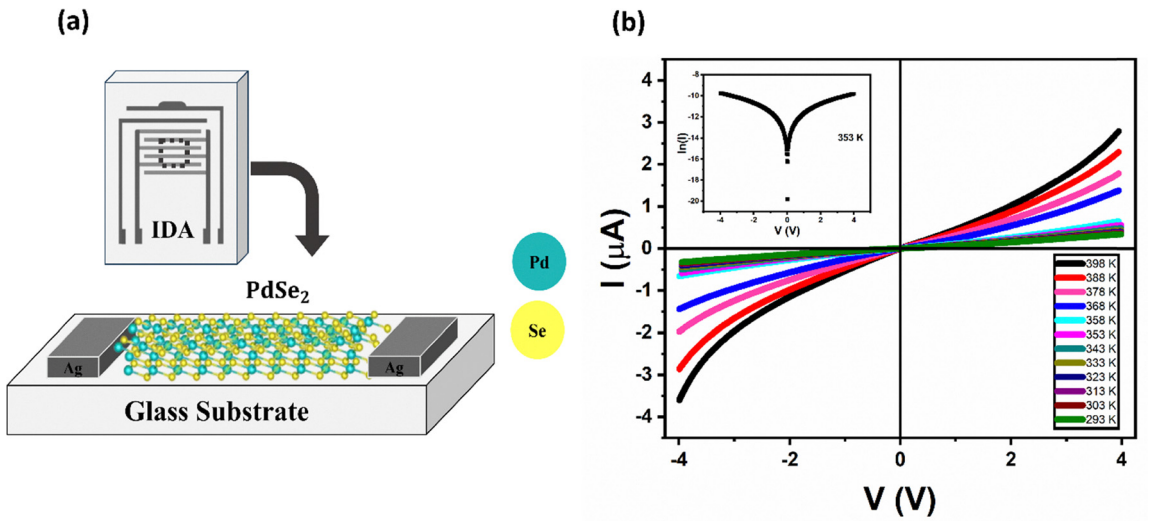


Fig. 2 (a) Schematic of the $PdSe_2$ flakes on IDA with silver contacts 10 μm apart on a glass substrate. (b) Temperature-dependent *I*–*V* characteristics plot of the $PdSe_2$ flakes in the temperature range of 293 K–398 K, showing a negative temperature coefficient.

result in nearly straight-line behavior in the plot, indicating that conduction in this regime is governed primarily by Schottky emission.

The thermionic emission model fits the forward biased current in the Schottky diode, as illustrated in Fig. 3(b), and it expresses the forward biased current as

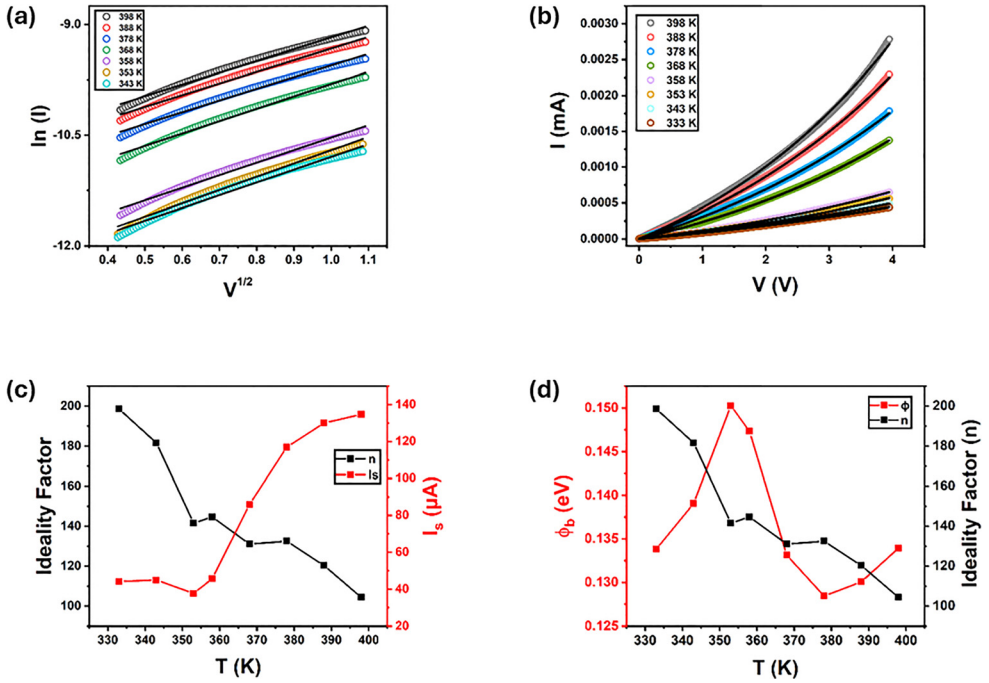


Fig. 3 (a) Plot of ln(*I*) *vs.* $V^{1/2}$ for Schottky emission fitting. (b) Equation fitting of the thermionic emission model. (c) Variation of the ideality factor and saturation current with temperature. (d) Modified Richardson's plot according to the Gaussian distribution of the barrier heights for $PdSe_2$.

follows:[15]

$$I = I_s\left[\exp\left(\frac{qV}{nk_BT}\right) - 1\right], \tag{2}$$

where $V$ denotes the applied voltage, $n$ is the ideality factor, $q$ is the electronic charge, $k_B$ is the Boltzmann constant, $T$ is the temperature and $I_s$ the saturation current. The saturation current is the reverse bias leakage current due to the minority charge carriers crossing the junction. It is expressed as follows:[15]

$$I_s = AA^*T^2\exp\left(-\frac{q\varphi_b}{k_BT}\right). \tag{3}$$

The Schottky barrier height can be expressed by molding the above equation as follows:

$$\varphi_b = \frac{k_BT}{e}\ln\left(\frac{AA^*T^2}{I_s}\right). \tag{4}$$

The fitted curves helped to evaluate the values of the saturation current and ideality factors for different temperatures using eqn (2). These values are plotted against temperature in Fig. 3(c). This plot helps gather the Schottky diode parameters that are necessary to establish possible device applications along with their performance. The ideality factor provides insight into the deviation of the device's behavior from that of an ideal diode. For an almost ideal case with low energy loss in semiconductors, an ideality factor close to 1 is required. A value greater than 1 can be attributed to the high electric field influencing the band. The ideality factor can be improved by taking measures towards improving the charge-carrier transport. The deduced values may allow for applications in heterojunction solar cells and photovoltaics.

Using these retrieved values, the barrier height was calculated using eqn (4) for different temperatures to be in the range of 0.128 eV–0.150 eV. The height of the potential barrier governs the degree of charge-carrier separation and associated energy losses. The nonlinear trend of barrier height $\varphi_b$ is attributed to barrier inhomogeneities and is characteristic of multiple conduction mechanisms taking place at different points along the curve, which can be improved by performing strain engineering, doping, *etc.* The temperature dependence of the barrier potential enables the device to serve not only as a sensor but also as a diagnostic platform for material characterization.[16]

Eqn (3) can also be modified to gain the value of Richardson's coefficient as follows:

$$\ln\left(\frac{I_s}{T^2}\right) = \ln(AA^*) - \frac{q\varphi_b}{k_BT}. \tag{5}$$

According to eqn (5), upon linear fitting of $\ln(I_s/T^2)$ *vs.* $1/T$, the intercept of the plot should give Richardson's coefficient. The obtained value of the coefficient was significantly smaller than the theoretical expectation. The considerable discrepancy between the calculated and expected values can be attributed to barrier inhomogeneities.[16] However, a corrected coefficient was determined by assuming a Gaussian distribution of the potential barrier heights, which introduces two new parameters: the mean barrier height ($\varphi_{b0}$) and the standard deviation ($\sigma$). These parameters are interrelated through the following expression:

$$\varphi_b = \varphi_{b0} - \frac{q\sigma^2}{2k_BT}, \tag{6}$$

where $\varphi_b$ is the experimentally determined value of the potential barrier height, whereas $\varphi_{b0}$ is to be measured using the expression above. When $\varphi_b$ is plotted against $1/T$, the slope renders the value of $\sigma$, which was 104.3 mV.

For the corrected value of Richardson's constant, we used the Gaussian corrected equation as follows:[17]

$$\ln\left(\frac{I_s}{T^2}\right) - \left(\frac{q^2\sigma^2}{2(k_BT)^2}\right) = \ln(AA^*) - \frac{q\varphi_b}{k_BT}. \quad (7)$$

Fig. 3(d) shows that the plot of $(\ln I_s/T^2) - (q^2\sigma^2/2(k_BT)^2)$ *vs.* $1/T$ is a straight line whose intercept was used to calculate the value of the modified Richardson's coefficient. The intercept returned 421 A cm$^{-2}$ K$^{-2}$ as the modified Richardson's coefficient and 0.322 eV as the mean barrier height. Since these values are well within the expected range, the assumption of a Gaussian distribution was validated.

In Fig. 4, the plot of $\ln(G)$ *vs.* $\sqrt{V}$ is illustrated for the temperature range of 348 K–398 K at voltages varying from 0 V to 2 V. It depicts the Poole–Frenkel emission where the electric field helps thermally weak, trapped charge carriers escape traps inside the potential valleys. PF emission obeys the following equation:[18]

$$I \approx V\exp\left(\frac{\beta_{PF}\sqrt{V} - \varphi_{PF}}{k_BT}\right), \quad (8)$$

where $\beta_{PF}$ is the lowering of the potential barrier height, and $\varphi_{PF}$ denotes the potential barrier. The linear fit of the plots provides strong evidence that PF emission leads the conduction of charge carriers from 0 V to 2 V. The slope of the plot provides the dielectric permittivity constant for the given temperature range according to the following expression:[14]

$$S = \frac{\sqrt{\frac{q^3}{d\varepsilon_0\varepsilon_r\pi}}}{k_BT}, \quad (9)$$

where $k_B$ is the Boltzmann constant, $d$ is the electrode spacing, $\varepsilon_0$ is the permittivity of free space, $\varepsilon_r$ is the dielectric permittivity and $q$ is the electronic charge. The inset of Fig. 4 depicts the change in the dielectric constant $\varepsilon_r$ with an increase in temperature from 348 K to 398 K. The average value of $\varepsilon_r$ came to be around 8, which is well within the expected range. The dielectric constant of $PdSe_2$ is moderate in terms of polarizability. Therefore, moderate screening of the external field by the charge carriers is expected. The variation in the dielectric constant is due to the thermally activated release of trapped charges, enhancing the polarization and screening ability of the material. The moderate yet tunable dielectric response highlights the potential of $PdSe_2$ for temperature-sensitive applications, like memristors and neuromorphic devices. With the enhanced channeling abilities evident, $PdSe_2$ may also find applications in solar energy devices and memristors.

To delve deeper into the electrode and grain properties of the $PdSe_2$ device, complex impedance spectroscopy was performed in a temperature range of 293 K–343 K at different frequencies. In Fig. 5(a), Nyquist plots between the values of $Z''$ and $Z'$ measured for the selected frequency domain are plotted. An equivalent circuit was designed using the Z-view software and is displayed in the inset of Fig. 5(a). It consists of an R-CPE circuit showing the crystalline nature of $PdSe_2$. The complex impedance of a system is given by the following:[19]

$$Z^* = Z' - jZ'', \quad (10)$$

where $Z'$ and $Z''$ are the real and imaginary parts of the complex impedance, respectively, which are then further individually expressed as follows:[20]

$$Z' = \left[\frac{R}{1+(\omega RC)^2}\right], \quad (11)$$

$$Z'' = \left[\frac{\omega CR^2}{1+(\omega RC)^2}\right], \quad (12)$$

where $\omega$ = angular frequency, $R$ is the resistance and $C$ is the capacitance of the device. The Nyquist plots exhibit a decrease in resistance as the temperature increases, which is a characteristic of semiconductors with a negative temperature coefficient of resistance. Considering that $PdSe_2$ acts as a semiconductor when the number of layers is $\sim$5 layers or less, it is consistent with the AFM values determined for this $PdSe_2$ device. The Nyquist plots were fitted using an equivalent circuit in Z-view, and the simulated curves showed excellent agreement with the experimental data (Table 1). As the temperature increases, the reduction in resistance is attributed to the enhanced probability of thermally activated detrapping of

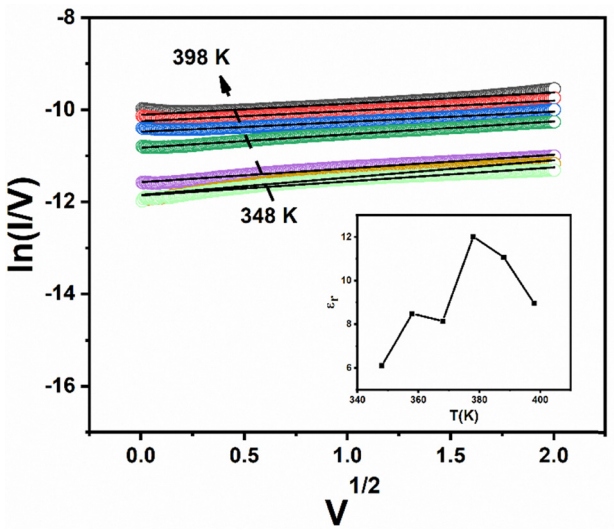


Fig. 4 Ln($I/V$) *vs.* $V^{1/2}$ plot for the Poole–Frenkel emission at temperatures of 348 K–398 K; with the inset showing the variation of the dielectric constant.

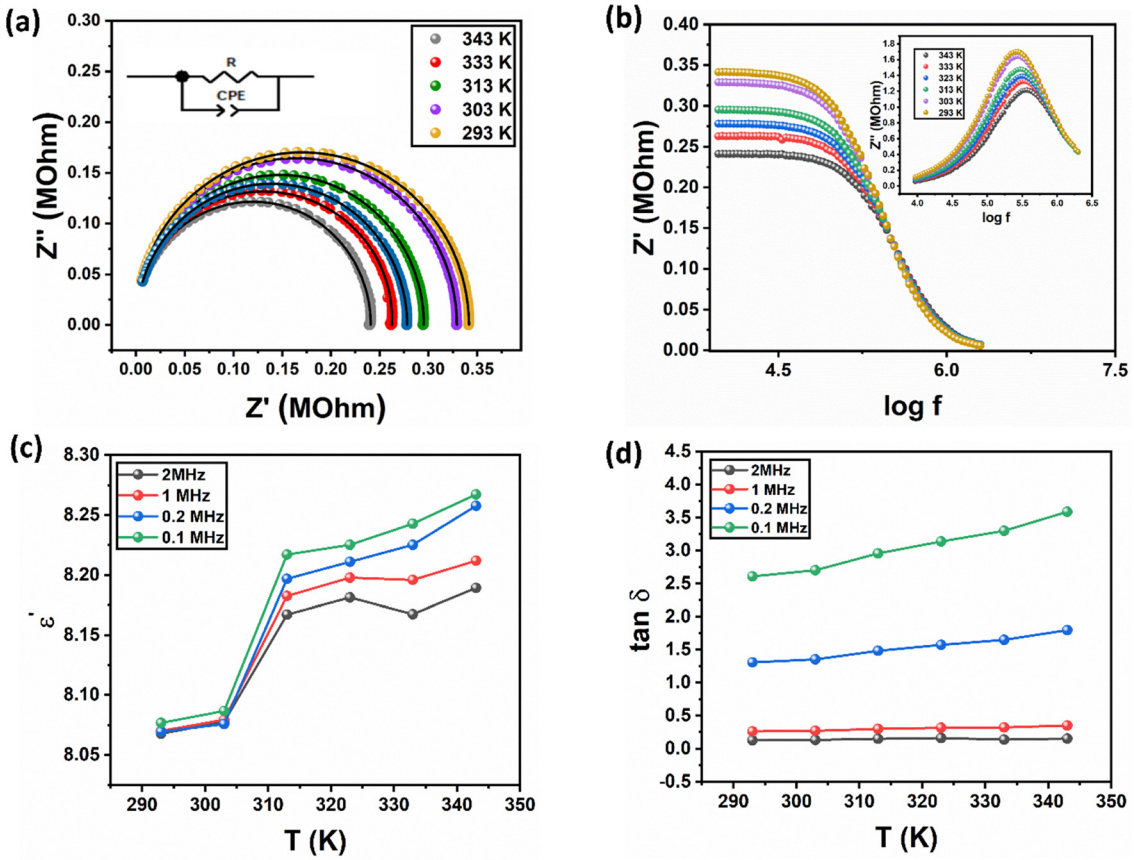


Fig. 5 (a) Nyquist plots of the $PdSe_2$ flake in the temperature range of 293 K–343 K, along with the circuit fittings, and the inset showing the equivalent circuit containing a resistance ($R$) and a constant phase element (CPE) connected in parallel. (b) Variation of $Z'$ with frequency in the temperature range of 293 K–343 K; and the inset exhibiting the behavior of $Z''$ with frequency in the temperature range of 293 K–343 K. (c) Trend of $\varepsilon'$ with temperature at specific values of frequency. (d) Trend of $\tan\delta$ with temperature at specific values of frequency.

Table 1 Z-View fitted parameters of the model (R-CPE) at specific temperature values

| Temperature (K) | Resistance $R$ (ohms) | Capacitance $C$ (pF) | $n$ |
|---|---|---|---|
| 343 | $2.418 \times 10^5$ | 1.847 | 1.0 |
| 333 | $2.634 \times 10^5$ | 1.833 | 0.9 |
| 323 | $2.783 \times 10^5$ | 1.825 | 0.87 |
| 313 | $2.955 \times 10^5$ | 1.821 | 0.92 |
| 303 | $3.291 \times 10^5$ | 1.795 | 0.88 |
| 293 | $3.413 \times 10^5$ | 1.779 | 0.79 |

charge carriers from defect states, increasing the free carrier concentration and effective mobility. The subsequent decline in total resistance with further temperature elevation clearly indicates a negative temperature coefficient, thereby reaffirming the semiconducting behaviour of the material.

Fig. 5(b) illustrates the decreasing trend of the real part of impedance ($Z'$) with increasing frequency over the temperature range of 293 K–343 K. At lower frequencies, $Z'$ exhibits negligible frequency dependence; however, as the frequency increases, a more pronounced decline is observed, and the $Z'$ values corresponding to different temperatures converge at higher frequencies. This behavior is attributed to the enhanced mobility of charge carriers and the resulting decrease in space-charge resistance, denoting improved electrical conduction in the upper frequency domain. The inset of Fig. 5(b) shows the varying trend of $Z''$ with the increase in frequency. The plot displays a rise in magnitude with increasing frequency, reaching a distinct peak, followed by a sharp decline that gradually converges as the frequency continues to increase. The decrease in $Z''$ is attributed mainly to the increased thermal activity. The peaks correspond to a certain value of frequency known as the relaxation frequency, $f_0$. The values of $f_0$ increase with the increase in temperature, indicating an enhanced conduction of the localized charge carriers through hopping, with the widening of peaks being a contribution from the temperature dependence of the relaxation mechanism.

Understanding the dielectric properties of a material is essential as it reveals the conduction mechanisms, polarization behavior, and dielectric relaxation processes that determine the device performance.[21] The polarization response of a material is inherently determined by its electronic, ionic, and interfacial characteristics, each of which shifts significantly with changes in frequency and temperature. The dielectric permittivity $\varepsilon^*$ has two parts, *i.e.*, real and imaginary, with the former usually referred to as the dielectric constant. It is expressed as follows:[19]

$$\varepsilon^* = \varepsilon' - j\varepsilon''. \quad (13)$$

The real part $\varepsilon'$ and the imaginary part $\varepsilon''$ are then further represented as follows:

$$\varepsilon' = \frac{t}{\omega A \varepsilon_0}\left(\frac{Z''}{Z'^2 + Z''^2}\right), \quad (14)$$

$$\varepsilon'' = \frac{t}{\omega A \varepsilon_0}\left(\frac{Z'}{Z'^2 + Z''^2}\right), \quad (15)$$

where $A$ is the cross-sectional area of the flake, $t$ is its thickness, $\varepsilon_0$ is the free space permittivity, and $Z'$ and $Z''$ are the real and imaginary parts of impedance, respectively. In our case, the area is approximately $A = 1 \times 10^{-10}$ m and the thickness of the flake is $\sim$4 nm. Using these values, the $t/A$ ratio was calculated to be 40 $m^{-1}$.

In Fig. 5(c), the plot between dielectric permittivity $\varepsilon'$ *vs.* $T$ for a temperature range of 293 K–343 K at specific frequencies shows a decrease in dielectric permittivity with an increase in frequency at all temperatures. This is because the interfacial polarizations are screened out at higher frequencies, leaving behind only the ionic and electronic polarizations. The interfacial polarizations, as key contributors, see an overall rise at lower frequencies due to better adaptation to field reversal, but they drop at higher frequencies due to their inability to cope with the rapidly changing field. The contribution from other polarizations, however, becomes evident at higher frequencies, but still, the net polarization declines.

Fig. 5(d) depicts the change in the dielectric loss $\tan\delta$ with temperature at specified frequencies. The dielectric loss is dependent on both parts of the dielectric permittivity and is represented as follows:[20]

$$\tan\delta = \frac{\varepsilon''}{\varepsilon'}. \quad (16)$$

Since $\varepsilon'$ and $\varepsilon''$ are both parts of the same entity, they increase and decrease under the same conditions, and the dielectric loss shows a similar trend. Therefore, as the temperature increases, the loss also increases due to enhanced thermal activity. This loss decreases with an increase in frequency, and the number of defects carrying charges also decreases.[20]

In Fig. 6(a), the change in the calculated values of $M'$ with changing $M''$ is demonstrated for a temperature range of 293 K–343 K. The two parameters are related by the following eqn (18):

$$M^* = M' + jM'', \quad (17)$$

where $M^*$ is the dielectric complex modulus, $M'$ is the real part of the modulus related to energy storage and $M''$ is the imaginary part that reflects loss. These two are then further expressed as follows:

$$M' = \left(\frac{\varepsilon'}{\varepsilon'^2 + \varepsilon''^2}\right), \quad (18)$$

$$M'' = \left(\frac{\varepsilon''}{\varepsilon'^2 + \varepsilon''^2}\right), \quad (19)$$

where $\varepsilon'$ and $\varepsilon''$ are the real and imaginary parts of the dielectric constant, respectively. Complex modulus is often employed as an analytical tool to understand the relaxation mechanisms in a system. It helps elucidate the suppression of electrode polarization and enhances bulk relaxation. It gives clear insights into charge carrier dynamics and relaxation mechanisms.

Complex electrical modulus provides valuable information about a material's electrical response, revealing how varying polarization mechanisms behave under changing electric fields and temperatures. In Fig. 6(a), a single semicircular arc is visible at all measured temperatures, exhibiting a slight movement toward higher $M''$ values as the temperature rises. This shift suggests that the modulus resistance decreases with rising temperature, which is in good agreement with previously reported findings.[22] Fig. 6(b) illustrates the trend of $M'$ with varying frequency for a temperature range of 293 K–343 K. At low frequencies, minimal electrode polarization occurs, as the decreased effective restoring force is insufficient to control charge carrier motion under the applied electric field, resulting in very small $M'$ values.[23] As frequency increases, $M'$ gradually rises and peaks at higher frequencies, signifying the presence of relaxation dynamics in the $PdSe_2$ flake throughout the studied range. The maximum $M'$ value, however, diminishes with rising temperature. Since $M'$ reflects the capacity of the material to store electrical energy, its reduction at elevated temperatures indicates improved charge-carrier mobility within the system.

In the inset of Fig. 6(b), $M''$ is plotted against frequency for a temperature range of 293 K–343 K. A broad relaxation peak appears for $M''$, moving toward higher frequencies as temperature rises. This shift signifies a thermally activated relaxation process, where the frequency span under the peak represents the range of long-distance charge carrier mobility.[24] The frequency at which a relation peak is observed is the characteristic frequency, $f_{max}$. Below $f_{max}$, the charge carriers can easily cover the polarization length, but beyond $f_{max}$, the charge carriers cannot travel the polarization length, and they become localized. As the temperature increases, the charge carriers gain energy and, thereby, relax relatively more slowly, while the peak shifts towards increasing frequency. This shift from long-range mobility to short-range mobility is evident in the $M''$ plot.[25]

Fig. 6(c) represents the response of complex modulus, demonstrating scaling behavior through a plot of $M''/M''_{max}$ *vs.* $\ln(f/f_{max})$. As the plotline climbs towards the peak, the charge carriers get restricted to their potential wells. The peak itself is evidence of the transition of long-range movement to short-range movement. Moreover, the plot for different temperatures overlapping shows that the relaxation mechanisms are receiving equal thermal support.[20]

In Fig. 6(d), the variation of $Z''$ and $M''$ with frequency provides valuable insight into the underlying relaxation mechanisms of the material. The two trendlines approach one another closely but do not overlap, signifying the coexistence of both localized relaxation processes and long-range conduction elements in $PdSe_2$.[26]

## Conclusion

In this work, $PdSe_2$ flakes exfoliated from a bulk crystal using TRT and transferred onto silver IDA contacts were analyzed

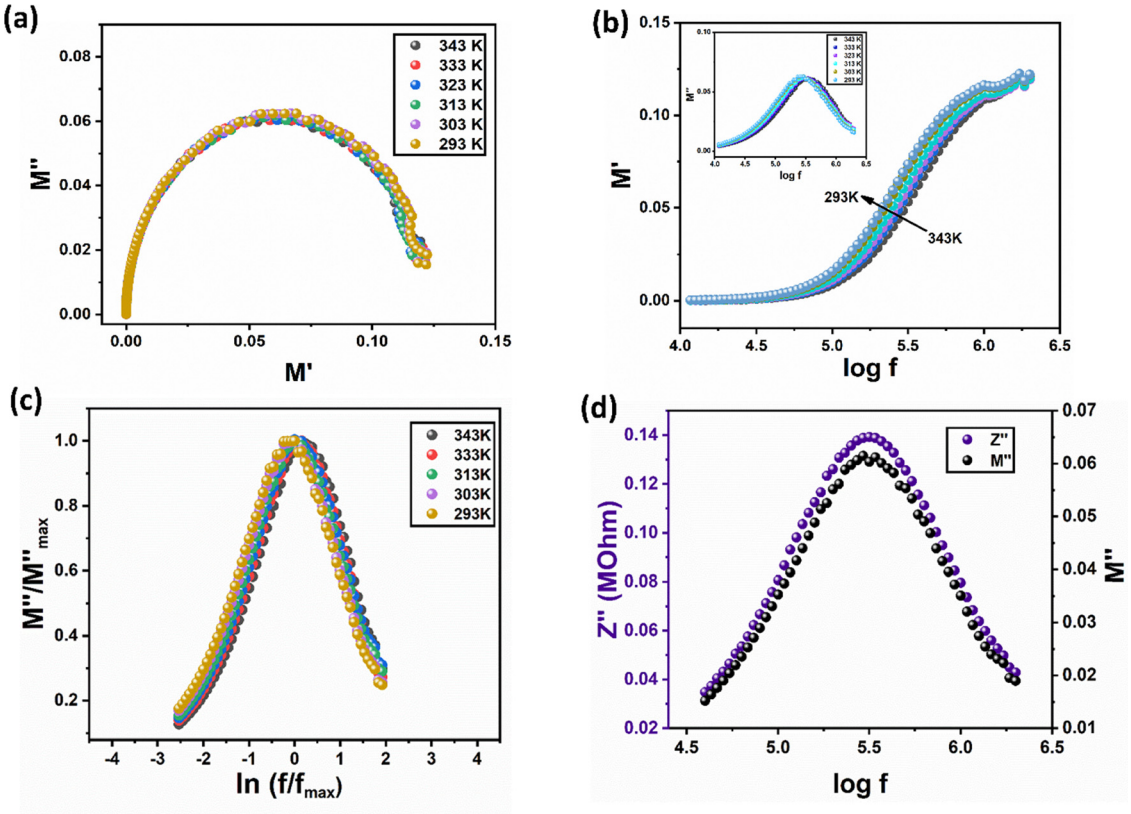


Fig. 6 (a) $M'$ *vs.* $M''$ plots of the mechanically exfoliated $PdSe_2$ flake in the studied temperature range. (b) Behavior of $M'$ with frequency at different temperatures; with the inset showing the behavior of $M''$ with frequency at different temperatures. (c) $M''/M''_{max}$ *vs.* $\ln(f/f_{max})$ plot at specific temperatures. (d) Comparison between $Z''$ and $M''$ with frequency at a specific temperature of 323 K.

through temperature-dependent AC and DC transport mechanisms at temperatures between 293 K and 398 K. Both bulk-limited and contact-limited conduction mechanisms were observed. These include Schottky and PF emissions. The Schottky emission was investigated, and the thermionic emission model was used to find the diode parameters and their trends with varying temperature. This device has shown a decrease in ideality factor, an increase in saturation current and an inhomogeneous barrier height with an increase in temperature. The analysis of PF emission revealed the dielectric constant to be in the range of 7–10. The investigation of complex impedance and modulus helped in determining the behavior of relaxation mechanisms and the trend of dielectric permittivity in response to the changing polarity of the field. This study reinforces the suitability of $PdSe_2$ for high-performance nanoelectronics and optoelectronic applications and provides insights for optimizing device architectures. This work, therefore, contributes significantly to the broader understanding of Pd-based transition metal dichalcogenides and their role in next-gen 2D material technologies.

## Conflicts of interest

There are no conflicts to declare.

## Data availability

The data that support the findings of this study are available from the corresponding author upon reasonable request.

## References

1 A. A. Tedstone, D. J. Lewis and P. O'Brien, Synthesis, Properties, and Applications of Transition Metal-Doped Layered Transition Metal Dichalcogenides, *Chem. Mater.*, 2016, **28**(7), 1965–1974.
2 J. A. Wilson and A. D. Yoffe, The transition metal dichalcogenides discussion and interpretation of the observed optical, electrical and structural properties, *Adv. Phys.*, 1969, **18**(73), 193–335.
3 S. Manzeli, D. Ovchinnikov, D. Pasquier, O. V. Yazyev and A. Kis, 2D transition metal dichalcogenides, *Nat. Rev. Mater.*, 2017, **2**(8), 17033.
4 Y. Wang, L. Zhou, M. Zhong, Y. Liu, S. Xiao and J. He, Two-dimensional noble transition-metal dichalcogenides for nanophotonics and optoelectronics: Status and prospects, *Nano Res.*, 2022, **15**(4), 3675–3694.
5 A. D. Oyedele, S. Yang, L. Liang, A. A. Puretzky, K. Wang and J. Zhang, *et al.*, PdSe2: Pentagonal Two-Dimensional Layers with High Air Stability for Electronics, *J. Am. Chem. Soc.*, 2017, **139**(40), 14090–14097.

6 W. Leong Chow, P. Yu, F. Liu, J. Hong, X. Wang and Q. Zeng, *et al.*, High Mobility 2D Palladium Diselenide Field-Effect Transistors with Tunable Ambipolar Characteristics, *Adv. Mater.*, 2017, **29**(21), 1602969.

7 M. Long, Y. Wang, P. Wang, X. Zhou, H. Xia and C. Luo, *et al.*, Palladium Diselenide Long-Wavelength Infrared Photodetector with High Sensitivity and Stability, *ACS Nano*, 2019, **13**(2), 2511–2519.

8 Y. Wang, J. Pang, Q. Cheng, L. Han, Y. Li and X. Meng, *et al.*, Applications of 2D-Layered Palladium Diselenide and Its van der Waals Heterostructures in Electronics and Optoelectronics, *Nano-Micro Lett.*, 2021, **13**(1), 143.

9 A. A. Puretzky, A. D. Oyedele, K. Xiao, A. V. Haglund, B. G. Sumpter and D. Mandrus, *et al.*, Anomalous interlayer vibrations in strongly coupled layered PdSe 2, *2D Mater.*, 2018, **5**(3), 035016.

10 J. Yu, X. Kuang, J. Li, J. Zhong, C. Zeng and L. Cao, *et al.*, Giant nonlinear optical activity in two-dimensional palladium diselenide, *Nat. Commun.*, 2021, **12**(1), 1–9.

11 Y. Li, L. Loh, S. Li, L. Chen, B. Li and M. Bosman, Anomalous resistive switching in memristors based on two-dimensional palladium diselenide using heterophase grain boundaries, *Nat. Electron.*, 2021, **4**, 348–356.

12 E. Park, J. E. Seo, G. Noh, Y. Jo, D. Y. Woo and I. S. Kim, *et al.*, A pentagonal 2D layered PdSe2-based synaptic device with a graphene floating gate, *J. Mater. Chem. C*, 2022, **10**(43), 16536–16545.

13 A. Di Bartolomeo, A. Pelella, X. Liu, F. Miao, M. Passacantando and F. Giubileo, *et al.*, Pressure-Tunable Ambipolar Conduction and Hysteresis in Thin Palladium Diselenide Field Effect Transistors, *Adv. Funct. Mater.*, 2019, **29**(29), 1902483.

14 U. Ali, Q. Abbas, S. M. T. Kazmi, M. H. Bhatti, F. Sher and M. A. Rafiq, Charge conduction in chalcopyrite CuFeS2 nanoflakes, *Ceram. Int.*, 2025, **51**(18), 26098–26106.

15 S. M. T. Kazmi, Z. Zahoor, N. T. Yusra, M. H. Bhatti, M. F. Afsar and F. Sher, *et al.*, Diode paremeters extraction and study of space charge limited current in (Ag, Au)/CoS2 Schottky diodes, *Phys. B*, 2023, **670**, 415400.

16 C. P. Y. Wong, C. Troadec, A. T. S. Wee and K. E. J. Goh, Gaussian Thermionic Emission Model for Analysis of Au/$MoS_2$ Schottky-Barrier Devices, *Phys. Rev. Appl.*, 2020, **14**(5), 054027.

17 A. Tataroğlu and F. Z. Pür, The Richardson constant and barrier inhomogeneity at Au/Si3N4/n-Si (MIS) Schottky diodes, *Phys. Scr.*, 2013, **88**(1), 015801.

18 Q. Abbas, S. M. T. Kazmi, C. Li, X. Xu and M. A. Rafiq, Charge transport mechanisms of PbSnSe2 and observation of transition from direct to Fowler–Nordheim tunneling, *RSC Adv.*, 2024, **14**(9), 5812–5816.

19 J. H. Joshi, D. K. Kanchan, M. J. Joshi, H. O. Jethva and K. D. Parikh, Dielectric relaxation, complex impedance and modulus spectroscopic studies of mix phase rod like cobalt sulfide nanoparticles, *Mater. Res. Bull.*, 2017, **93**, 63–73.

20 S. M. T. Kazmi, Q. Abbas, C. Li, X. Xu and M. A. Rafiq, Temperature and frequency dependence of conductivity, density of states, and dielectric permittivity of ternary metal chalcogenide PbSnSe2 flake, *Ceram. Int.*, 2024, **50**(14), 25763–25770.

21 C. B. Mohamed, K. Karoui, S. Saidi, K. Guidara and A. B. Rhaiem, Electrical properties, phase transitions and conduction mechanisms of the [(C2H5)NH3]2CdCl4 compound, *Phys. B*, 2014, **451**, 87–95.

22 X. Wang, J. Zhuang, Q. Peng and Y. Li, A general strategy for nanocrystal synthesis, *Nature*, 2005, **437**(7055), 121–124.

23 P. B. Macedo, The role of ionic diffusion in polarisation in vitreous ionic conductors, *Phys. Chem. Glasses*, 1972, **13**, 171–179.

24 C. V. Chanmal and J. P. Jog, Dielectric relaxations in PVDF/BaTiO3 nanocomposites, *eXPRESS Polym. Lett.*, 2008, **2**, 294–301.

25 W. Ben Nasr, A. Mahmoud, F. Boschini and A. Ben Rhaiem, Optical and AC conductivity studies on Li2-xRbx MoO4 ($x$ = 0, 0.5, 1) compounds, *J. Alloys Compd.*, 2019, **788**, 522–532.

26 Z. Imran, M. A. Rafiq, M. Ahmad, K. Rasool, S. S. Batool and M. M. Hasan, Temperature dependent transport and dielectric properties of cadmium titanate nanofiber mats, *AIP Adv.*, 2013, **3**(3), 032146.